Experimental study of the thermal performance of chaotic geometries for their use in PEM fuel cells

Cathy Castelain, Yahia Lasbet, Bruno Auvity, Hassan Peerhossaini

For submission to the International Journal of Thermal Sciences, October 2015

Experimental study of the thermal performance of chaotic geometries for their use in PEM fuel cells

Cathy CASTELAIN[a*], Yahia LASBET[a], Bruno AUVITY[a], Hassan PEERHOSSAINI[b]

[a]Laboratoire de Thermocinétique de Nantes, CNRS-UMR 6607, Polytech Nantes, University of Nantes, BP 50609, 44306 Nantes cedex 3, France

[b]Laboratoire Interdisciplinaire des Energies de Demain, CNRS-UMR 8236, Univ. Paris Diderot, Sorbonne Paris Cité, Paris, France

[*](corresponding author: cathy.castelain@univ-nantes.fr)

Abstract

In order to improve the thermal performance of heat exchangers used in the bipolar plates of PEM fuel cells, we suggest replacing the networks of straight channels by geometries generating chaotic flows. In transport applications, high heat densities are generated because of the combined high heat fluxes and the imposed compactness of heat exchangers. Moreover, the convective regime in the cooling channels is laminar and the channel network has to be as thin as possible to limit the electrical resistance through the bipolar plates. In such extreme conditions, the generation of spatial chaos by geometrical perturbation in the heat exchanger is a relevant way to intensify heat transfer. In this paper, an experimental study is presented for two chaotic advection geometries and a straight tube. A specialized test bench was designed and built. The channels were placed in a counterflow heat exchanger with a laminar flow in the center and a turbulent flow in the annulus. Heat exchange was carefully analyzed to obtain the convective heat transfer coefficient for each channel.

Nomenclature

A_c Cross-sectional surface area, m^{-2}
C_1 Constant of the Rose correlation
C_2 Constant of the Rose correlation
Cp Specific heat, $J.kg^{-1}.K^{-1}$
dp/ds Local pressure gradient, $Pa.m^{-1}$
D_h Hydraulic diameter, m
E Efficiency
$\dot{E}$ Exergy flux
ex Exergy, $J.kg^{-1}$
f Friction coefficient
h Heat transfer coefficient, $W.m^{-2}.K^{-1}$
H_g Overall convective heat transfer coefficient, $W.m^{-2}.K^{-1}$
L Hydrodynamic length, m
l_{ex} Exergy destruction, $J.kg^{-1}$
LMTD, Log mean temperature difference for a heat exchanger, K
$\dot{m}$ Flow rate, $m^3.s^{-1}$
Nu Nusselt number
Po Poiseuille number
Pr Prandtl number
$\dot{Q}$ Heat flux, W
Re Reynolds number
R_w Conduction resistance, $W^{-1}.m^2.K$
s Curvilinear coordinate, m
S Exchange surface area, m^2
T Temperature, K
Um Bulk velocity, $m.s^{-1}$

Greek symbols

η_{ex} Exergy efficiency
λ Conductivity, $W.m^{-1}.K^{-1}$
ρ Density, $kg.m^{-3}$
μ Dynamic viscosity, $kg.m^{-1}.s^{-1}$
v Kinematic viscosity, $m^2.s^{-1}$
λ Flux density, $W.m^{-2}$

Subscripts and superscripts

1 Primary
2 Secondary
e Inlet
Ext External
In Ingoing
m Bulk mean
O Reference
Out Outgoing
s Outlet
W Wall

1. Introduction

Fossil resources constitute the world's main energy source. Their increasing consumption, their limited nature and their considerable impact on the environment have promoted research into alternative clean and renewable energies, including the use of fuel cells. A fuel cell is an electrochemical reactor that behaves like a continuous current generator. It benefits from several advantages, such as high efficiency (around 50%), reliability, low pollution emission (water being the only residue of the electrochemical reaction if hydrogen is used as the fuel), and low noise level. It can be integrated into a portable system for autonomous electricity production if it has its own fuel reserve. A Proton Exchange Membrane (PEM) fuel cell is a low temperature cell, see Figure 1, constituted of a polymer membrane as the electrolyte with a working temperature of around 80°C. Currently, it is one of the most developed fuel cell technologies, along with the Solid Oxide Fuel Cell (SOFC, working temperature of 800°C).

Thermal management is a key issue for the PEM fuel cell, Kandlikar and Lu [1]. The optimum performance of the electrolyte requires a well-defined temperature range. Beyond this range, the membrane is quickly degraded, thus a cooling system must be inserted in the bipolar plates. These plates serve as electrical connectors between cells placed in series in a stack as well as a flow distributor for the reacting gas and cooling liquid, Hermann et al. [2]. Figure 1(a) shows a diagram of two cells in series in a stack. The central component is the bipolar plates where the flow field for reactants and the channels for the cooling liquid can be seen. The theoretical efficiency of the fuel cell is 80% but in practice it is about 50%, see Hussain et al. [3]. Therefore, the thermal power produced in the cell by the electrochemical reaction is of the same order as the electric power and must be removed by the cooling system to avoid overheating and thus membrane deterioration.

PEM fuel cell cooling systems can be classified according to the power produced, Larminie and Dicks [4], Zhang and Kandlikar [5].

If the fuel cell power is below 100 W, the air flow coming from the external environment for the cathode supply is sufficient to extract most of the heat released by the reaction without the need for a cooling ventilator. Thermal transfer from the cell to the surroundings also occurs by natural convection. Koschany [6] developed a PEM fuel cell stack in which the bipolar plates consist of anisotropic graphite and are larger than the cell, hence heat is removed by fin effects.

For a fuel cell power between 100 W and 2-3 KW, the humidification level of the exchanging proton membrane is lower than 26% if the cooling system and the supply system are on the same circuit, Larminie and Dicks [4]. In these conditions, the proton exchange

membrane dehydrates. It is thus essential to separate the air supply circuit from the cathode of the air cooling circuit. The air flow is cooled by a ventilator. Liu et al. [7] have numerically simulated a PEM fuel cell stack, showing that the temperature gradient inside the stack is mostly determined by the air flow cooling.

Beyond 5 KW, air cooling is insufficient and the use of cooling water circulation becomes inevitable. The good thermal and mechanical properties of the bipolar plates enable the liquid to circulate and thus the thermal power generated by the chemical reaction to be removed. The optimization of the cooling system becomes essential because, on one hand, the fuel cell performance is markedly affected by the internal temperature gradient and, on the other hand, the fuel cell system efficiency may be greatly reduced by an excessive energy consumption by the cooling system (pressure drop).

The cooling systems studied in the literature may be classified into two types: one with a phase change through the use of a heat pipe, Meyer [8], Koehler et al. [9], Rullière et al. [10], Clement and Wang [11], and one without a phase change (forced monophasic convection). The latter is the most common and, in this type, the cell is cooled by a coolant (water) circulating inside the bipolar plates, see Figure 1(b) and 1(c). The classic cooling system consists of parallel straight tubes (Voss and Chow [12]), or serpentine channels (Li and Sabir [13]). Exploring the parallel serpentine type, Asghari et al. [14] conducted a numerical study to find the number of channels to be placed in parallel: they showed that the higher the number, the lower the pressure drop but the higher the temperature non-uniformity within the bipolar plate. Reiser [15] patented a system that can simultaneously manage the membrane cooling and the evacuation of water produced by the cathode during the electrochemical reaction. This system is made of porous hydrophilic plates, which are installed on both sides of the proton exchange membrane. In these plates, the water flow cools the membrane, moistens its pores and, at the same time, removes the water produced by injecting it into the coolant circuit. In order to simplify and reduce the price of the stack manufacture, Chow et al. [16] incorporated the cooling system and the gas supply system into one integrated system. This has the potential to reduce the fuel cell volume and consequently increase the stack power. Sasmito et al. [17] conducted a computational study comparing parallel, serpentine, oblique-fins, coiled, hybrid parallel serpentine and parallel-serpentine-oblique-fins as coolant channels. They showed that the serpentine-based coolant channel exhibits the best thermal management while inducing the highest pressure drop and thus the highest parasitic loss. They concluded that innovative coolant channels, like these various hybrid designs, have the potential to satisfy both thermal and power consumption criteria.

Taking as a starting point the flows in the respiratory system, a new design for cooling electronic chips based on a constructal approach was studied, Chen and Cheng [18]. Senn and Poulikakos [19] have numerically characterized the convective heat transfer and the pressure losses of a cooling network based on a constructal drawing for PEM fuel cell application. They have shown that the constructal network decreases the pressure losses and increases the heat transfer compared to a serpentine channel with the same heat-exchange surface area.

The study of the hydrodynamic conditions inside the heat exchangers used in the bipolar plates of PEM fuel cells shows that the flow regime is laminar (Reynolds number below 500). By anticipating a future reduction in fuel cell size, it is clear that the dimensions of the exchanger and the internal flow Reynolds number are going to decrease too. It is well known that the laminar flow regime is not very favorable for intense heat transfer exchanges. One way to intensify the heat transfer in this regime is to produce Lagrangian chaos, otherwise called chaotic advection, from a deterministic flow by simple geometrical perturbations. Since the first work of Aref on two-dimensional periodical flows, Aref [20], many authors have studied the improvement in mass transport by chaotic advection in different flow configurations, Jones et al. [21], Castelain et al. [22], Khakhar et al. [23]. Chaotic advection has also been proved to be an efficient way to transport heat, Acharya et al. [24], Mokrani et al. [25]. Chaos can be created in a laminar regime in an open flow simply by introducing a geometrical perturbation judiciously placed.

At the macroscale, “twisted-pipe” configurations have proved to be very effective mixers for Re >60. Liu et al. [26] presented a microchannel design based on the “twisted pipe” and the mixing performance of the flow in this channel for a Reynolds number between 6 and 70. Beebe et al. [27] presented the paradigm of “designing for chaos” as a general framework for improving mixing in microfluidic applications. They designed a passive in-line micromixer, which relies on three degrees of freedom to create chaos. The mixer design was fabricated using a compression micromolding process to create three-dimensional flow channels in polydimethylsiloxane (PDMS). Computational and experimental analyses demonstrated the effectiveness of the resulting design in generating chaos in the flow and hence improving mixing.

The constraints for the compact heat exchanger to be machined in the bipolar plates are the following:

- to remove the heat flux due to the high power density reached in transport applications,

- to reduce temperature gradients within the fuel cell. Each membrane electrode assembly (MEA) constituting a cell is designed to operate in optimal conditions. Besides gas flux conditions (mass flow, humidity, pressure), the MEA temperature is crucial, thus temperature gradients must be avoided.
- the exchanger must be essentially flat to minimize the electrical resistance,
- the pressure drop across the heat exchanger must be low (overall fuel cell efficiency),
- the flow regime is laminar,
- the exchanger should be relatively easy to make (low cost and time of machining).

Heat management is thus essential for the PEMFC. In a previous work, Lasbet et al. [28, 29] proposed various channel geometries with the ability to generate chaotic flows as potential candidates for insertion in a heat exchanger. Using CFD, such geometries were characterized in terms of both their thermal performance (Nusselt number) and their hydrodynamic performance (Poiseuille number). Lasbet et al. [29] presented the evolution of two particle trajectories, which are initially close to each other and injected at the inlet of different configurations (zigzag, C-shaped, V-shaped and B-shaped). In the square-wave mixer channel, the flow is regular and the particle trajectories do not diverge. In the C-shaped channel, the particle trajectories can diverge rapidly, a clear sign of chaotic advection, as in the article of Liu et al. [26]. In the V-shaped and B-shaped channels, the particle divergence also shows chaotic behavior.

In order to complete the study and validate the numerical approach, an experimental study, reported here, was undertaken on a selection of geometries. The aim was to develop a reliable experimental device associated with an adequate methodology to characterize the heat transfer performance of chaotic geometries for application in fuel cell cooling. The paper is organized as follows: Section 2 is devoted to the presentation of the various geometries envisaged and the main computational results. Section 3 presents the experimental set-up, the methodology used to obtain the convective heat transfer coefficient, and the instrumentation. Finally, the experimental results for the different configurations are presented in Section 4 and conclusions are drawn in Section 5.

2. Description of the geometries studied and the numerical results

The first part of the work was devoted to the design of a three-dimensional geometry able to induce chaotic advection. The objective was thus to benefit from chaotic advection without introducing a large three-dimensional geometry, as the heat exchanger has to be essentially flat. Therefore, the extent of the geometries is mainly 2D, with a third dimension that is at least an

order of magnitude lower than the other two dimensions. This challenge led to the study of geometries with a basic design called a period, which is repeated in the direction of the flow. Figure 2 presents the selected designs, for which only one period is shown. They are all made up from a succession of curved and straight segments with elevation between two segments. A multiplicity of designs is possible based on these alternatives, the goal being to find those that increase the heat transfer with the minimum pressure loss. In order to give an example of a cooling heat exchanger based on these geometries, Figure 3 presents a parallel arrangement of cooling channels, each of them being constituted of a succession of C-shaped periods.

To qualify these geometries, numerical simulations were carried out. For all geometries, the channel cross-section is rectangular with an aspect ratio of 2 (2 mm by 1 mm). The hydraulic diameter D_h is thus equal to 1.33 mm. Every geometry is periodic in space, hence the computational domain is limited to one period. Each period has an unfolded length equal to 0.018 m. Geometries are compared with equal unfolded lengths but not with equal heat-exchange surface areas, for different period numbers. The non-dimensional parameter that characterizes the flow regime is the classic Reynolds number, defined as:

$$\mathrm{Re} = \frac{U_m . D_h}{\upsilon} \tag{1}$$

where ν is the kinematic viscosity of the fluid ($\nu = 15.10^{-6}$ m^2 s^{-1} for water) and U_m is the bulk velocity:

$$U_m = \frac{1}{A_c} . \iint_{A_C} u . dA_c \tag{2}$$

and A_c is the cross-sectional surface area.

The thermal performance of all geometries is characterized by the evolution of the Nusselt number, Nu, along the curvilinear coordinate s. Nu is defined as:

$$Nu = \frac{\varphi}{T_W - T_m} . \frac{D_h}{\lambda} \tag{3}$$

where T_w is the channel wall temperature, λ the thermal conductivity of the flowing fluid (here water, λ = 0.6 W/m.K) and T_m the bulk mean fluid temperature over the cross-sectional area of the channel:

$$T_m = \frac{1}{A_C.U_m}.\iint_{A_C} u.T.dA_C \tag{4}$$

The hydrodynamic performance of all geometries is characterized by the evolution along the curvilinear coordinate s of the friction coefficient f, defined as:

$$f = -\left(\frac{dp}{ds}\right).\frac{D_h}{\frac{1}{2}.\rho.U_m{}^2} \tag{5}$$

where ρ is the fluid density and dp/ds is the local pressure gradient along the curvilinear coordinate of the channel. Since this parameter depends on the Reynolds number, it is preferable to follow the evolution of the product f.Re, which is the Poiseuille number Po. All details of calculations can be found in Lasbet et al. [28, 29].

For each geometry, the thermal performance was characterized for a Reynolds number of 200 by local and mean Nusselt number evaluation, and by imposing a uniform flux density of 10,000 W/m^2. The hydrodynamic performance was characterized by the calculation of the local and average Poiseuille number. The ratio between the average Poiseuille number and the average Nusselt number was used to compare the hydrodynamic and thermal performances. The lower this ratio, the better the compromise between heat transfer intensification and pressure loss reduction.

Another criterion was considered to characterize these geometries in terms of energy efficiency. It is based on a second law analysis using exergy, see Akpinar [30], Borel and Favrat [31]. The exergy balance in the case of a tube heated with constant flux is written as:

$$\dot{I}_{ex} = -\Delta \dot{ex}_{es} + \iint_e^S \left(1 - \frac{T_0}{T_w}\right) \delta\dot{Q}\, dS = T_0.\dot{s}_{gen} \quad [\mathrm{W}] \tag{6}$$

where $\dot{I}_{ex}$ is the exergy destruction due to irreversibilities, $\Delta \dot{ex}_{es}$ is the exergy variation of the working fluid (here water) between the inlet and outlet of the tube and the term $\iint_e^S \left(1 - \frac{T_0}{T_w}\right) \delta\dot{Q}\, dS$ is the available heat introduced along the heated wall of the tube. In this term, T_w is the local wall temperature and $\delta\dot{Q}$ is the local heat flux density, here equal to 10,000 W/m^2. An exergy efficiency can be introduced, Yilmaz et al. [32]:

$$\eta_{ex} = \frac{\sum \dot{E}_{out}}{\sum \dot{E}_{in}} \tag{7}$$

where $\dot{E}_{out}$ and $\dot{E}_{in}$ are the outgoing and ingoing exergy fluxes, respectively. In the particular case of convective heat transfer in a tube, this exergy efficiency is written as follows (the reference state is assumed equal to the inlet state of the working fluid, $T_0 = T_e$):

$$\eta_{ex} = \frac{\Delta \dot{e}x_{es}}{\iint_e^s \left(1-\frac{T_0}{T_w}\right)\delta\dot{Q}dS} = 1 - \frac{T_0.\dot{s}_{gen}}{\iint_e^s \left(1-\frac{T_0}{T_w}\right)\delta\dot{Q}dS} \quad (8)$$

An efficient heat exchange is characterized by a high η_{ex}.

In Table 1, the average Nusselt number, the average Poiseuille number, the ratio between these two numbers and the exergy efficiency are presented for all the geometries considered. Geometries are ranked from the lowest value of Po/Nu to the highest. The lowest value of the Po/Nu ratio is obtained with the V-shaped geometry. The B-shaped, zigzag-3D and U-shaped geometries also present an interesting compromise, slightly better than that of the C-shaped geometry. The highest exergy efficiency is obtained with the C-shape, closely followed by the B-shape, zigzag-3D, V-shape and U-shape.

The asymptotic value of the Nusselt number for the straight tube is equal to 3.03. This is very close to the theoretical value of 3.02 (Shah and London, [33]). For the zigzag-2D geometry, a secondary flow structure (Dean cells) is generated along a bend due to centrifugal force. At the exit of each bend, the orientation of the centrifugal force changes, inducing a rotation change of these cells without any destruction. The presence of this secondary flow increases the local Nusselt number, which oscillates around a mean value of 8.23 and which is better than that obtained in the straight tube configuration.

The geometry C-2D, studied by Liu et al. [26], also presents a better heat transfer intensification compared to a straight tube. The flow during one C-2D period is characterized by two elementary stages: secondary flow intensification near the two singularities and its attenuation in the right part separating the two singularities. The C geometry can create chaotic trajectories. For each C-shape period, two three-dimensional space perturbations are present. Each perturbation is made up of three successive 90° bends. The local average Nusselt number values obtained in the C-shaped geometry are higher than those obtained in the other geometries. The Nusselt number mean value in the C geometry is 19.40, which represents a considerable heat transfer increase compared to the three other geometries. Other chaotic geometries (Figure 2 d-g) were thermally characterized and showed thermal performances rather higher than the straight tube. The difference between these geometries lies in the geometrical perturbation and the distance between two successive perturbations. The thermal feature of these geometries relies on their spatial complexity, which destroys the boundary layer and prevents its reconstitution. As the boundary layer is a barrier against wall heat transfer, its

destruction increases heat transfer. However, the pressure losses due to the presence of singularities are higher than those in a straight tube.

In the second law analysis, the mechanical irreversibilities due to flow friction (pressure loss) contribute only slightly to the overall irreversibilities, which are mainly dominated by thermal irreversibilities. The main reason is that the flow regime is laminar. Therefore, the highest exergy efficiency is obtained with the geometry offering the highest Nusselt number, without regard to the Poiseuille number.

This numerical study revealed that the V-shaped and C-shaped geometries presented the best thermal features. These were thus chosen to be studied experimentally, along with the straight tube as a reference.

3. Presentation of the experimental device and the associated measurement techniques

3.1 Experimental device

To guarantee a level of geometrical and metrological quality in the experimental device, a scale ratio of 10 was applied to the real size of the experimental stack typical of PEMFC channels (rectangular section: 2 mm by 1 mm). This scale change required some precautions, which are linked to the similitude theory.

In order to characterize thermally the geometries considered, it was decided to place them in the center of a counterflow heat exchanger. A diagram of the experimental set-up is presented in Figure 4 showing the different elements. Figure 5 is a photograph of the heat exchanger in which the geometry studied (here C-shaped) can be seen.

The counterflow heat exchanger is constituted of two branches: (i) the cold one flowing in the center of the heat exchanger is the internal part of the studied geometry. It is hereafter called the primary circuit; (ii) the hot branch flows outside the studied geometry and is called the secondary circuit (external loop).

All the geometries have the same entrance section, which has an aspect ratio of 2, a height of 1 cm, and a width of 2 cm (D_h=1.33 cm). In the C geometry, a straight part, 2 cm long, is present at the entrance and at the exit. The main element in this geometry is the series of four 90° curved ducts. Each curvature plane is moved 90° in relation to the curvature plane of the previous one. A straight 4-cm length is positioned between the second and third curved duct. Each basic element is constituted by five parallelepiped blocks as represented in Figure 2.

In the V geometry, built on the same concept, the curved ducts have a curvature angle of 45°. This change in angle, compared to the C geometry, is intended to reduce the heat losses. The lengths of the straight duct were chosen to give an identical unfolded length in both cases. The geometries are made in stainless steel with a thickness of 1 mm and are constituted of 5 basic elements described below. The unfolded length for each basic element is 18 cm. The envelope, where the secondary fluid passes, follows the shape of the primary circuit and has a constant hydraulic diameter of 1 cm. The outside wall is in Plexiglas.

The secondary fluid circuit is essentially a closed loop from and back to a 160-liter water reservoir. A three-way valve is used on the return circuit to divert the secondary flow to a mass balance in order to measure the flow. Most of the time, the secondary loop is closed. The fluid passes through a Grundfos CR4-20 centrifugal pump, which ensures flows ranging between 0 and 100 l/min using a valve to regulate the flow. In order to maintain the fluid temperature in the secondary circuit, an electrical resistance is used to heat the secondary flow before it returns to the tank. The regulation at around 0.5°C is ensured by a PID controller. The primary fluid is the one to be heated in the heat exchanger. From a PVC tank, the fluid passes through a pump that provides flows ranging between 0 and 4 l/min. This pump is equipped with a variable speed drive to adjust the flow rate. At the exchanger exit, water is recovered in a tank and is continuously weighed in order to measure the flow rate using a precision balance. The fluid circulates inside the studied geometries, see Figure 5. A straight length is placed upstream of the heat exchanger to ensure an established velocity profile at the test section entry. The non-dimensional theoretical establishment length, L, for a rectangular straight tube of aspect ratio equal to 2 is given in Table 2, Shah and London [33]. The non-dimensional establishment length, L, is equal to 0.45 for small Reynolds numbers and 0.09 for large Reynolds numbers. A static mixer (SULZER® SMX made up of 5 elements (DN 20)) is inserted at the exit of the primary circuit to obtain the mixing temperature. Thermocouples of type K, 80 µm in diameter, are placed at the entrance and exit of the primary and secondary fluid circuits. The flow rates of these two circuits are measured by two precision balances connected to an acquisition station.

3.2. Exchanger characterization

The heat exchanger is thermally insulated with rockwool. The thermal losses are estimated by the following relation:

$$Heat\ losses = \left(1 - \left|\left(\frac{\dot{Q}_2}{\dot{Q}_1}\right)\right|\right) \times 100 \quad (9)$$

$\dot{Q}$ is the heat flux exchanged between the two circuits. The subscripts “2” and “1” refer to the secondary and primary circuits, respectively. The thermal losses are about 10%.

The overall convective heat transfer coefficient, H_g, is given by the following formula for a counterflow exchanger:

$$H_g = \frac{\dot{Q}}{S_i\ LMTD} = \frac{\dot{m}_1\ c_{p1}(T_{1s} - T_{1e})}{S_1\ LMTD} = \frac{\dot{m}_2\ c_{p2}(T_{2e} - T_{2s})}{S_1\ LMTD} \tag{10}$$

$$LMTD = \frac{(T_{2s} - T_{1e}) - (T_{2e} - T_{1s})}{\ln(T_{2s} - T_{1e}) - \ln(T_{2e} - T_{1s})} \tag{11}$$

$LMTD$ is the log mean temperature difference for a counterflow exchanger. The total thermal resistance of a heat exchanger is the sum of three resistances in series:

$$\frac{1}{H_g} = \frac{1}{h_1} + R_w + \frac{S_1}{h_2 S_2} \tag{12}$$

where h_2 is the convective heat exchanger coefficient between the external wall and the secondary fluid, h_1 is the convective heat exchanger coefficient between the internal wall and the primary fluid, S_2 is the external surface area of the considered geometry near the hot fluid, S_1 is the internal surface area of the considered geometry near the cold fluid ($S_1/S_2 \approx 1$) and R_w is the conduction resistance through the wall geometry. To obtain the experimental value of H_g, the four temperatures T_{1e}, T_{2e}, T_{1s} and T_{2s} and the flow rate $\dot{m}_1$ have to be measured.

Finding h_1 necessitates the estimation of h_2. In order to have a small error in the determination of h_1, h_2 has to be as high as possible. This condition implies a strong turbulent secondary flow, which tends to impose the wall temperature. To estimate h_2, the relation of Dittus-Boelter [34] for a turbulent flow (Re > 2500) in circular piping (Padet [35] and Feidt [36]) is used:

$$Nu_2 = \frac{h_2 D_{h2}}{\lambda_2} = 0.024\ Re_2^{0.8}\ Pr^{0.3} \tag{13}$$

Based on the two preceding equations, the uncertainty in the determination of h_1 due to the temperature measurement accuracy can be estimated and is presented in Figure 6. The precision of h_1 is primarily driven by the estimation of LMTD. If the secondary Reynolds number becomes too high, the temperature difference T_{2s}-T_{2e} cannot be measured with precision. At a fixed secondary Reynolds number, if the primary Reynolds number becomes too high, the temperature difference T_{1s}-T_{1e} cannot be measured with precision. If the primary Reynolds number is too low, the temperature difference T_{2e}-T_{1s} becomes too small to be estimated with precision. However, a precision of less than 3% in the determination of h_1 can be achieved with our experimental apparatus.

The external heat transfer coefficient, h_2, varies with the secondary circuit Reynolds number for a monophasic turbulent flow according to the following law (Rose [37]):

$$h_2 \alpha \, Re_2^{0.8} \tag{14}$$

In this case, equation (12) can be written as follows:

$$\frac{1}{H_g} = C_1 \, Re_2^{-0.8} + C_2 \tag{15}$$

where the constant C_2 represents the sum of the conduction resistance and the internal exchange resistance. Equation (15) shows that $1/H_g$ decreases with the secondary flow Reynolds number. With high secondary Reynolds numbers, the thermal resistance $\frac{S_1}{h_2 S_2}$ becomes negligible and the evolution of $1/H_g$ tends towards an asymptotic value that is equal to C_2. The knowledge of the conduction resistance enables the internal heat transfer coefficient, h_1, to be deduced. The secondary fluid temperature varies slightly between the inlet and the outlet. Consequently, this exchanger can be compared to an imposed wall temperature heat exchanger. In this case, the experimental results can be compared with those found numerically for an imposed wall temperature.

3.3. Qualification of the experimental device

The measured flow rate showed a standard deviation of about 0.01 kg/s for the highest value of the secondary flow and 0.0003 kg/s for the smallest value. These results cause uncertainties of about 2%. The standard deviation for the primary circuit flow rate values was around 10^{-6} kg/s. Thus, the uncertainty of the primary flow rate measurement was about 10^{-4} %.

The four temperatures T_{1e}, T_{2e}, T_{1s} and T_{2s} used to characterize the heat exchanger were recorded once the thermal stationary state was reached. The dispersion of the temperature values was about 0.05°C.

The measurement reproducibility was verified by carrying out three identical tests: the secondary Reynolds number was equal to 3300 and the primary flow Reynolds number varied from 100 to 550. Figure 7 represents the evolution of the overall heat transfer coefficient, H_g, for a straight duct with the primary flow Reynolds number for the three tests. The overall heat transfer coefficient shows a decreasing dispersion, which varies with the Reynolds number from 7% to 0.7%. This shows that the overall heat transfer measurement is perfectly reproducible.

Heat exchanger efficiency E can be estimated. It is defined by the following relation:

$$E = \frac{\dot{Q}_1}{\dot{Q}_{max}} \tag{16}$$

with $\dot{Q}_1 = \dot{m}_1 c_{p1}(T_{1s} - T_{1e})$ and $\dot{Q}_{max} = \dot{m}_1 c_{p1}(T_{2e} - T_{1e})$ being the maximum heat flux that can be received by the primary flow. Figure 8 presents the evolution of the exchanger efficiency for the straight geometry for the same three tests versus the primary fluid Reynolds number. The three tests are almost identical and dispersion can thus be considered negligible.

4. Experimental results

4-1. Appearance of mixed convection in the three geometries

To check the potential presence of mixed convection in each of the three geometries (straight channel, V-shaped and C-shaped), the overall heat exchanger coefficient, H_g, was evaluated for two different secondary inlet circuit temperatures, T_{2e}. Figure 9-a presents the evolution of H_g for the straight duct versus the Reynolds number, Re, for two secondary inlet temperatures, 50°C and 60°C, the primary fluid inlet temperature being 20°C in both cases. The overall heat transfer coefficient depends on the secondary inlet temperature. Therefore, the mixed convection regime is significantly present in the straight duct. This result is confirmed by the calculation of the Richardson number, which is 13.6 for the small values of primary Reynolds numbers and 0.6 for the large values. Figure 9-b presents the evolution of H_g for the V-shaped and C-shaped geometries with the Reynolds number under the same conditions. For each geometry (V-shaped and C-shaped), H_g evolution with the Reynolds number is independent of the secondary inlet temperature. The mixed convection regime is not observable with these geometries in the temperature range considered. Note that the calculation of the Richardson number in this kind of geometry is not possible. Therefore, based on the superposition of the curves for the overall heat transfer exchanger coefficient with two different temperatures, it is concluded that the flow regime in the V-shaped and C-shaped geometries is the forced convection mode, whereas in the straight tube, mixed convection is present.

4.2 Heat exchanger characterization

The results presented in this section concern the efficiency, the overall heat transfer coefficient and the internal heat transfer coefficient for the three geometries considered. The efficiency and the heat transfer coefficient were obtained for a secondary Reynolds number of 3300.

Efficiency

Figure 10 presents the evolution of the efficiency, E, for the straight, V-shaped and C-shaped geometries with the primary Reynolds number, Re_1. In the three geometries, the efficiency decreases with the Reynolds number. The higher the primary flow rate, the shorter the residence time and thus, the higher the fluid temperature difference between the inlet and the outlet. The flow structure in the two chaotic geometries (V-shaped and C-shaped) is chaotic (Lasbet et al., [29]), so the efficiency in these two geometries is better than that obtained in the straight tube. The efficiency of the C-shaped geometry is higher than that of the V-shaped geometry. Since chaotic advection exploits the kinematic effect of the secondary flows, it can be conjectured that the kinematic effect in the C-shaped geometry is stronger than in the V-shaped geometry.

Overall heat transfer coefficient

Figure 11 presents the overall heat transfer coefficient, H_g, for the straight, V-shaped and C-shaped geometries versus the primary Reynolds number. H_g obtained for the forced convection regime in the straight tube is calculated with equation (8). The heat exchanger boundary conditions are taken as a constant wall temperature. Therefore, the values of h_1 are obtained from the reference (Shah and London, 1978) for an imposed temperature condition.

The overall heat transfer coefficient in the two chaotic geometries is higher than that obtained with the straight tube, particularly in the forced convection regime. This thermal performance of the V-shaped and C-shaped geometries is due to the chaotic nature of their flows contrary to the flow in the straight tube, which is regular. The overall heat transfer coefficient of the C-shaped geometry is the highest. This could be due to a significant number of chaotic zones in this geometry compared to the V-shaped geometry. The increase in H_g in the chaotic geometries compared to the straight tube in the case of forced convection is calculated as follows:

$$Improvement\ in\ H_g = \frac{Hg(V\ or\ C) - Hg(straight\ tube)}{Hg(straight\ tube)} \times 100 \quad (17)$$

This improvement is plotted as a function of the Reynolds number in Figure 12. It can vary from 80% to 270% for the V-shaped geometry and from 130% to 385% for the C-shaped geometry.

Internal heat transfer coefficient

The determination of the internal heat transfer coefficient, h_1, consists of fixing the Reynolds number of the primary circuit, i.e. so that the internal heat transfer coefficient is constant, and varying the Reynolds number of the secondary circuit. The evolution of $1/H_g$ according to the Reynolds number of the secondary circuit tends towards an asymptotic value (C_2), which is equal to the sum of the conduction resistance and the internal convection resistance, see equation (10). Knowing the value of the conduction resistance, the value of the internal convection heat transfer h_1 can be determined and thus the internal Nusselt number.

The correlation coefficient R_2 and the standard error made on the constants C_1 and C_2 are calculated to determine the regression equations. This method was also used by Akpinar [30] to determine the regression equations in a counterflow heat exchanger study. Details of this method are presented in the work of Benelmir et al. [38] and Rose [37]. In our study, the standard error made on the constants C_1 and C_2 does not exceed 5%. On the other hand, the correlation coefficient (R_2) is given on each figure.

Figure 13 represents the evolution of the overall heat transfer resistance for the straight duct versus the secondary Reynolds number for a secondary inlet temperature of 50°C and for a primary Reynolds number of 450. The inverse of the overall heat transfer coefficient evolves with the Reynolds number according to the following equation:

$$\frac{1}{H_g} = 0.30\, Re_2^{-0.8} + 0.00159 \tag{18}$$

The constant 0.00159 $W^{-1}.m^2.K$ represents the sum of the inverse of the internal heat transfer coefficient and the conduction resistance in the straight tube. Since the latter is equal to 5. 10^{-5} $W^{-1}.K.m^2$, the internal convective heat transfer coefficient in the straight tube is equal to 649.48 $W.m^{-2}.k^{-1}$ and the Nusselt number is 14.39. The Nusselt number calculated numerically in a straight tube in a mixed convection regime for an imposed wall temperature condition of 50°C, and a Reynolds number of 450, is 13.76. The numerical and experimental values are thus very close and show a difference of about 5%.

Figure 14 presents the evolution of the overall resistance of the heat exchanger in the V-shaped and C-shaped geometries with the secondary Reynolds number for two secondary inlet temperatures of 40°C and 50°C and for a constant primary Reynolds number of 540. The constants 0.00097 $W^{-1}.m^2.K$, 0.00091 $W^{-1}.m^2.K$, 0.00065 $W^{-1}.m^2.K$ and 0.00062 $W^{-1}.m^2.K$ appear on the graphs. They represent the sum of the conduction resistance and the inverse of the internal convective heat transfer coefficient for each geometry and for the two temperatures.

The conduction resistance in the V-shaped and C-shaped geometries are 8.8 10^{-6} $W^{-1}.K.m^2$ and 2.3 10^{-5} $W^{-1}.K.m^2$, respectively. Therefore, the Nusselt number for each geometry and for the two secondary inlet temperatures can be obtained. The experimental values of the Nusselt number were compared to those obtained numerically for a Reynolds number of 540 and for an imposed wall temperature condition (40°C and 50°C) in a mixed convection regime. They are presented in Table 3. The evolution of the total exchanger resistance for the two temperatures is almost identical. This implies that mixed convection is not observable in the chaotic geometries in this temperature range. Generally, the experimental Nusselt values corroborate those resulting from the numerical study.

5. Conclusion and Perspectives

The traditional design of the cooling system incorporated in the bipolar plates of a PEM fuel cell stack consists of a simple network of parallel straight channels of depth equal to half or a third of the plate thickness. This cooling system will quickly reach its limits with the increasing power density of the PEMFC and a new design must be found. In this article, we have proposed a new type of geometry for the coolant channels, which can generate a spatially chaotic flow in a laminar regime. Such a design has the potential to improve significantly the thermal performance of the heat exchanger incorporated in the bipolar plates.

In this work, we designed and built an experimental device for the thermal characterization of the chaotic geometries considered. This device is similar to a counterflow heat exchanger. The thermal performance of the chaotic geometries (V-shaped and C-shaped) and that of a straight tube were measured. The measurements confirmed the numerical results, revealing a large increase in the internal convective heat transfer coefficient for the chaotic geometries compared to the straight tube. The experimental validation of the thermal performance of chaotic geometries is essential for their future use in industrial applications.

As far as PEM fuel cell applications are concerned, the next step will be the study of the thermal performance of the whole bipolar plate by the resolution of the coupled convection-conduction problem with a numerical and experimental approach.

Acknowledgment

This study was carried out within the framework of the PRI 3.1 CNRS: PEM Fuel cells and benefited from fruitful discussions in the French research grouping GDR CNRS 3339 PACS “Pile A Combustibles et Systèmes”. The authors thank Michel Jézégou for his help in the design of the experimental set-up.

References

[1] Satish G. Kandlikar, Zijie Lu, Thermal management issues in a PEMFC stack – A brief review of current status, Applied Thermal Engineering, Volume 29, Issue 7, May 2009, Pages 1276-1280.

[2] Allen Hermann, Tapas Chaudhuri, Priscila Spagnol, Bipolar plates for PEM fuel cells: A review, International Journal of Hydrogen Energy, Volume 30, Issue 12, September 2005, Pages 1297-1302.

[3] M.M. Hussain, J.J. Baschuk, X. Li, I. Dincer, Thermodynamic analysis of a PEM fuel cell power system, International Journal of Thermal Sciences, Volume 44, Issue 9, September 2005, Pages 903-911.

[4] J. Larminie, and A. Dicks, Fuel Cell Systems Explained. England: Wiley, 2003.

[5] Guangsheng Zhang, Satish G. Kandlikar, A critical review of cooling techniques in proton exchange membrane fuel cell stacks, International Journal of Hydrogen Energy, Volume 37, Issue 3, February 2012, Pages 2412-2429.

[6] P. Koschany (2001), Fuel cell stack with cooling fins and use of expanded graphite in fuel cells, Patent WO 01/54218 A2.

[7] Zhixiang Liu, Zongqiang Mao, Cheng Wang, Weilin Zhuge, Yangjun Zhang, Numerical simulation of a mini PEMFC stack, Journal of Power Sources, Volume 160, Issue 2, 6 October 2006, Pages 1111-1121.

[8] A. Meyer (1991). Solid polymer fuel cell system: high current density operation. Patent US 5,064,732.

[9] C.W. Koehler, G.V. Ommering, N.H. Puester, (1986), Active cooling system for electrochemical cells, Patent US 4,578,324.

[10] R. Rullière, V. Ayel, F. Lefèvre, G. Burban, A. Alexandre, M. Lallemand, (2007). Theoretical and experimental studies of two-phase heat spreader for PEM fuel cell cooling applications, Proceedings of 14th IHPC, Florianopolis, Brazil. 140

[11] Jason Clement, Xia Wang, Experimental investigation of pulsating heat pipe performance with regard to fuel cell cooling application, Applied Thermal Engineering, Volume 50, Issue 1, 10 January 2013, Pages 268-274.

[12] H. H. Voss, C. Y. Chow, (1993). Coolant flow field plate for electrochemical fuel cells, Patent US 5230966.

[13] Xianguo Li, Imran Sabir, Review of bipolar plates in PEM fuel cells: Flow-field designs, International Journal of Hydrogen Energy, Volume 30, Issue 4, March 2005, Pages 359-371.

[14] Saeed Asghari, Hooman Akhgar, Bagher Faghih Imani, Design of thermal management subsystem for a 5 kW polymer electrolyte membrane fuel cell system, Journal of Power Sources, Volume 196, Issue 6, 15 March 2011, Pages 3141-3148.

[15] C. Reiser (1997). Ion exchange membrane fuel cell power plant with water management pressure differentials. Patent 5700595.

[16] C. Chow, B. Wozniczka, J.K. Chan, (1998). Integrated reactant and coolant fluid flow field layer for an electrochemical fuel cell, Patent US 5804326.

[17] Agus P. Sasmito, Jundika C. Kurnia, Arun S. Mujumdar, Numerical evaluation of various gas and coolant channel designs for high performance liquid-cooled proton exchange membrane fuel cell stacks, Energy, Volume 44, Issue 1, August 2012, Pages 278-291.

[18] Yongping Chen, Ping Cheng, Heat transfer and pressure drop in fractal tree-like microchannel nets, International Journal of Heat and Mass Transfer, Volume 45, Issue 13, June 2002, Pages 2643-2648.

[19] S.M. Senn, D. Poulikakos, Laminar mixing, heat transfer and pressure drop in tree-like microchannel nets and their application for thermal management in polymer electrolyte fuel cells, Journal of Power Sources, Volume 130, Issues 1–2, 3 May 2004, Pages 178-191.

[20] Hassan Aref (1984). Stirring by chaotic advection. Journal of Fluid Mechanics, 143, pp. 1-21.

[21] Scott W. Jones, Oran M. Thomas and Hassan Aref (1989), Chaotic advection by laminar flow in a twisted pipe. Journal of Fluid Mechanics, 209, pp. 335-357.

[22] Cathy Castelain, Asen Mokrani, Yves Le Guer, Hassan Peerhossaini, Experimental study of chaotic advection regime in a twisted duct flow, European Journal of Mechanics - B/Fluids, Volume 20, Issue 2, March 2001, Pages 205-232.

[23] D.V. Khakhar, J.G. Franjione, J.M. Ottino, A case study of chaotic mixing in deterministic flows: The partitioned-pipe mixer, Chemical Engineering Science, Volume 42, Issue 12, 1987, Pages 2909-2926.

[24] Narasimha Acharya, Mihir Sen, Chang Hsueh-Chia, Heat transfer enhancement in coiled tubes by chaotic mixing, International Journal of Heat and Mass Transfer, Volume 35, Issue 10, October 1992, Pages 2475-2489.

[25] Asen Mokrani, Cathy Castelain, Hassan Peerhossaini, The effects of chaotic advection on heat transfer, International Journal of Heat and Mass Transfer, Volume 40, Issue 13, September 1997, Pages 3089-3104.

[26] R.H. Liu, M.A. Stremler, K.V. Sharp, Michael G. Olsen, J.G. Santiago, R.J. Adrian, H. Aref, D.J. Beebe, Passive mixing in a three-dimensional serpentine microchannel, Journal of Microelectromechanical Systems, Volume 9, Issue 2, June 2000, Pages 190-197.

[27] David J Beebe, Ronald J Adrian, Michael G Olsen, Mark A Stremler, Hassan Aref, Byung-Ho Jo, Passive mixing in microchannels: Fabrication and flow experiments, Mécanique & Industries, Volume 2, Issue 4, July–August 2001, Pages 343-348.

[28] Yahia Lasbet, Bruno Auvity, Cathy Castelain, Hassan Peerhossaini, A chaotic heat-exchanger for PEMFC cooling applications, Journal of Power Sources, Volume 156, Issue 1, 19 May 2006, Pages 114-118.

[29] Yahia Lasbet, Bruno Auvity, Cathy Castelain, Hassan Peerhossaini, Thermal and Hydrodynamic Performances of Chaotic Mini-Channel: Application to the Fuel Cell Cooling, *Heat Transfer Engineering,* volume 28 (8**),** 2007, Pages 795–803.

[30] Ebru Kavak Akpinar, Evaluation of heat transfer and exergy loss in a concentric double pipe exchanger equipped with helical wires, Energy Conversion and Management, Volume 47, Issues 18–19, November 2006, Pages 3473-3486.

[31] Lucien Borel, Daniel Favrat, Thermodynamique et Energétique : de l'énergie à l'exergie, PPUR Mécanique, 2005

[32] M. Yilmaz, O.N. Sara, S. Karsli (2001) Performance evaluation criteria for heat exchangers based on second law analysis, Exergy, an International Journal, vol(1), issue 4 Pages 278-294

[33] R. Shah, A. London, Laminar flow forced convection in ducts. New York: Academic Press, 1978.

[34] F.W. Dittus, L.M.K. Boelter, Heat transfer in automobile radiators of the tubular type, International Communications in Heat and Mass Transfer, Volume 12, Issue 1, January–February 1985, Pages 3-22.

[35] Jacques Padet, Convection thermique et massique, Nombre de Nusselt partie 1. Techniques de l'Ingénieur BE, 8206, 2006

[36] Michel Feidt, Thermodynamique et Optimisation Energétique des Systèmes et Procédés. Paris: Lavoisier, 1987.

[37] John W Rose, Heat-transfer coefficients, Wilson plots and accuracy of thermal measurements, Experimental Thermal and Fluid Science, Volume 28, Issues 2–3, January 2004, Pages 77-86.

[38] Riad Benelmir, Mohamed Khalfi, Michel Feidt, Identification du coefficient de transfert thermique sur la surface externe d'un échangeur de chaleur à tubes et ailettes planes en fonction de l'humidité de l'air, en l'absence de condensation, Revue Générale de Thermique, Volume 36, Issue 4, April 1997, Pages 289-301.

List of Tables

List of Figures

	Mean Nusselt number	*Mean Poiseuille number*	*Ratio*	*Exergy efficiency*
	Nu	$Po_m = f.Re$	Po_m/Nu	η_{ex}
Geometry V	14.03	88.4	6.3	23.5%
Geometry B	13.03	93.17	7.15	23%
Geometry Zigzag–3D	15.14	114.38	7.55	24%
Geometry U	17.73	137.51	7.75	25%
Geometry C	19.40	151.73	7.82	26%
Geometry Zigzag–2D	8.23	84.40	10.25	11%
Geometry C–2D	11.06	125.55	11.35	16%
Straight duct	3.03	62	20.46	6.5%

Table 1: Comparison of the average Nusselt number, the average Poiseuille number, and the ratio Po_m/Nu for all geometries considered

Wiginton and Dalton	Fleming and Sparrow	Han	McComas
0.085	0.095	0.066	0.025

Table 2: Values of the entry length for a rectangular straight geometry of aspect ratio equal to 2, Shah and London (1978)

Nu	T = 40°C	T = 50°C
V-shaped geometry (exp.)	35.4	37.1
V-shaped geometry (num.)	31.4	31.8
C-shaped geometry (exp.)	22.9	24.4
C-shaped geometry (num.)	22.6	23.0

Table 3: Experimental and numerical Nusselt numbers for two temperatures (Re_1=540)

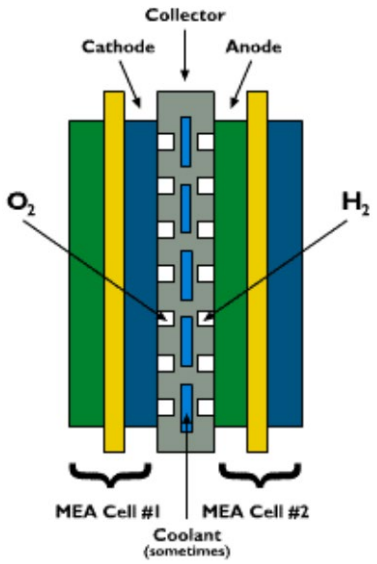

(a)

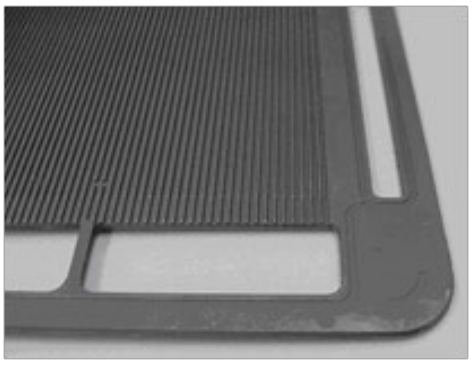

(b)

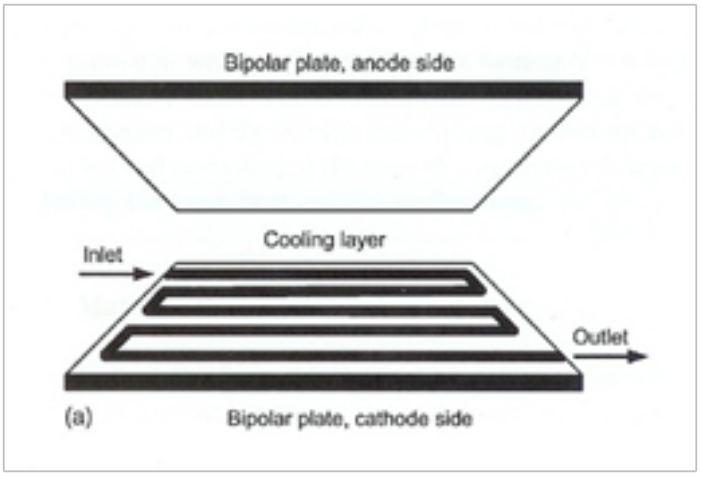

(c)

Figure 1: (a) Diagram of a PEM fuel cell,

(b) Photograph of a network of parallel cooling channels machined in a bipolar plate

(c) Diagram of a serpentine cooling channel, from Senn and Poulikakos (2004)

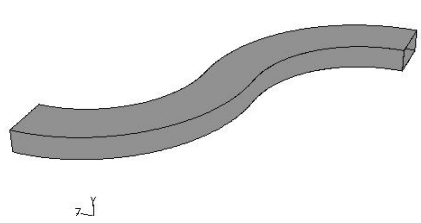

a) Zigzag-2D

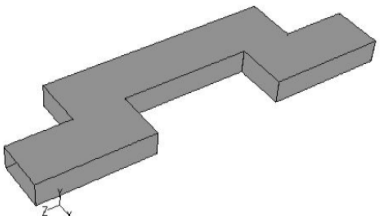

b) C-2D

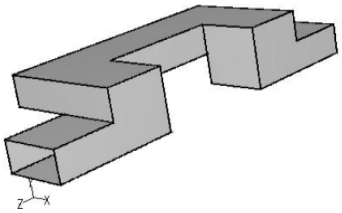

c) C

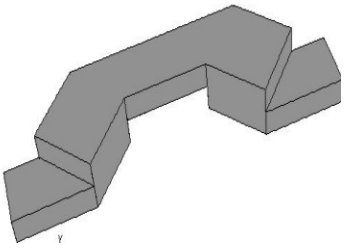

d) V

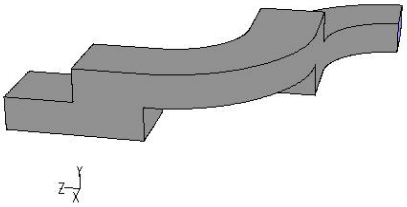

e) Zigzag-3D

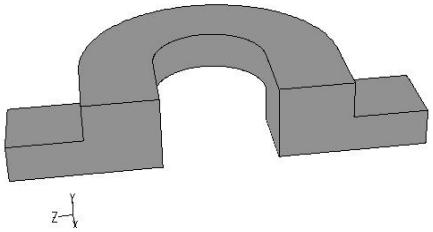

f) U

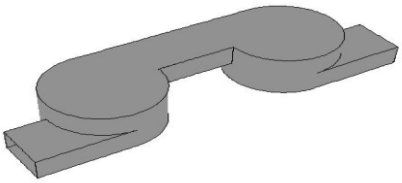

g) B

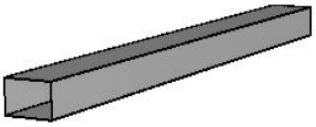

h) straight duct

Figure 2: Presentation of the geometries

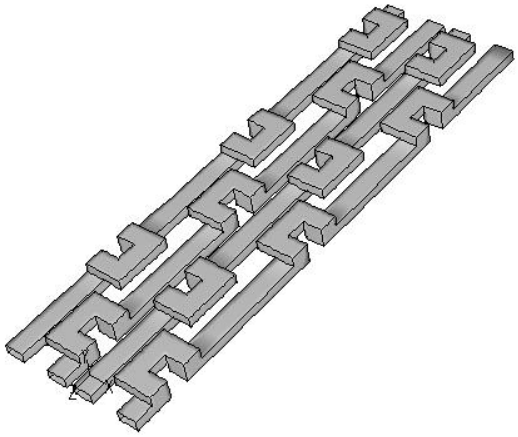

Figure 3: Example of a heat exchanger to be inserted into a PEMFC bipolar plate composed of a parallel arrangement of channels based on a C-shaped period

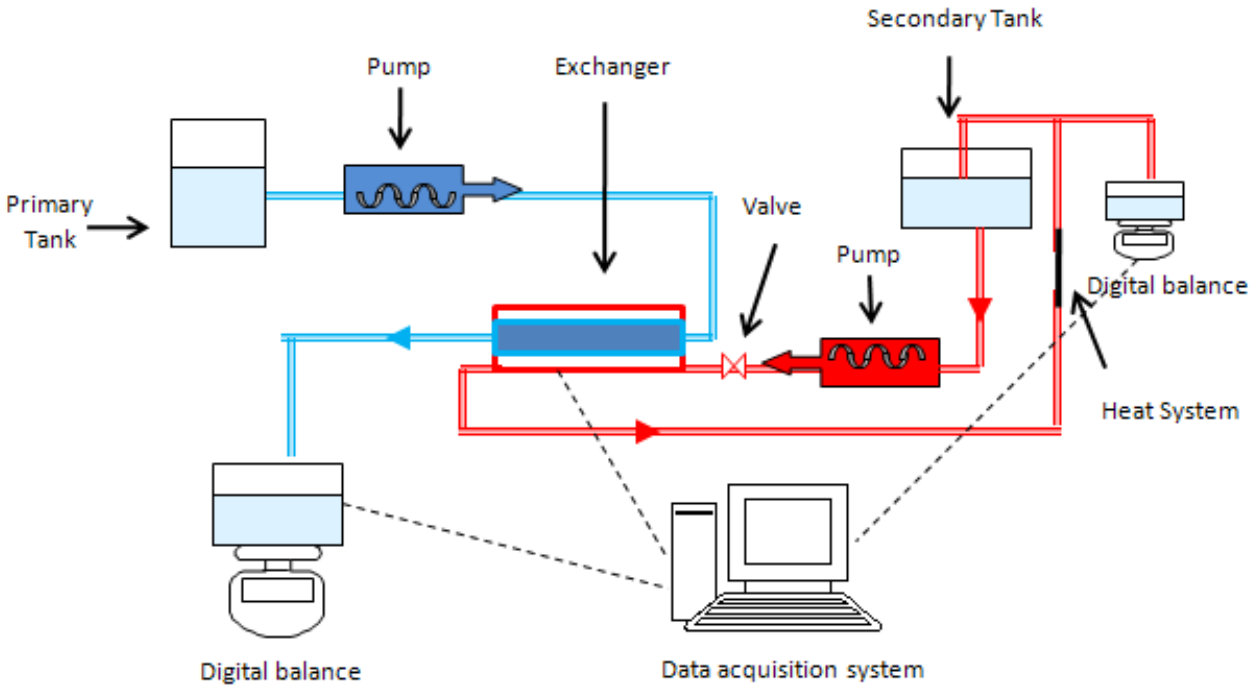

Figure 4: Diagram of the experimental device

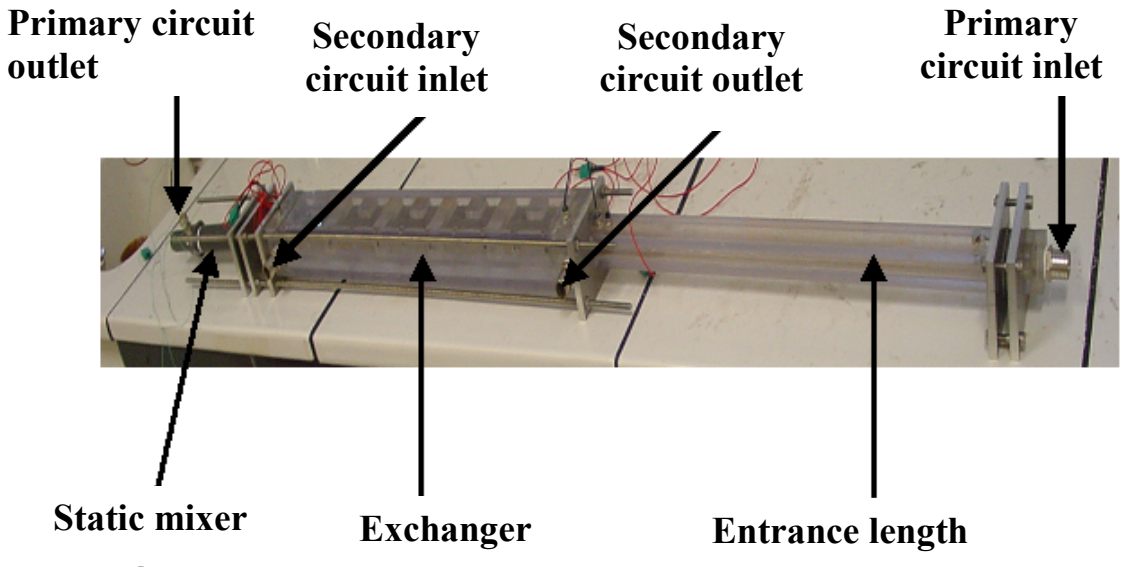

Figure 5: Photograph of the experimental heat exchanger

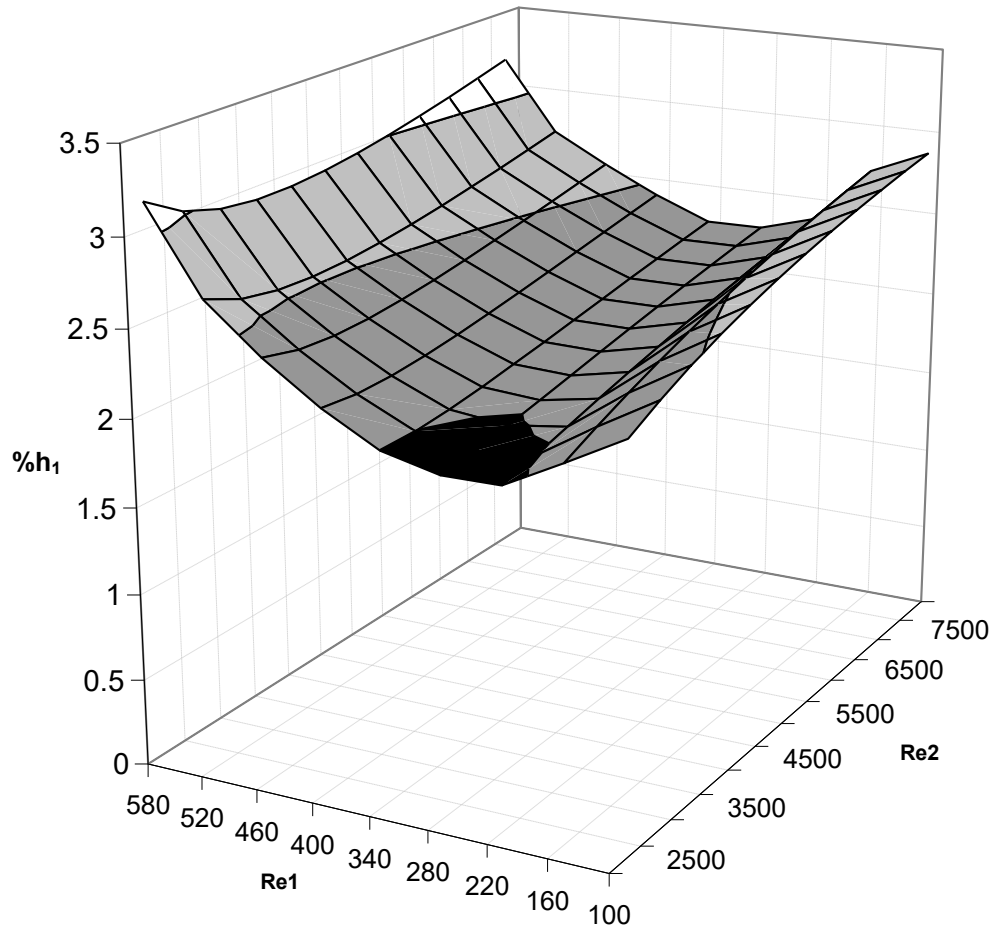

Figure 6: Evolution of uncertainty about the internal convective heat transfer coefficient (h_1) versus primary (Re_1) and secondary (Re_2) Reynolds numbers

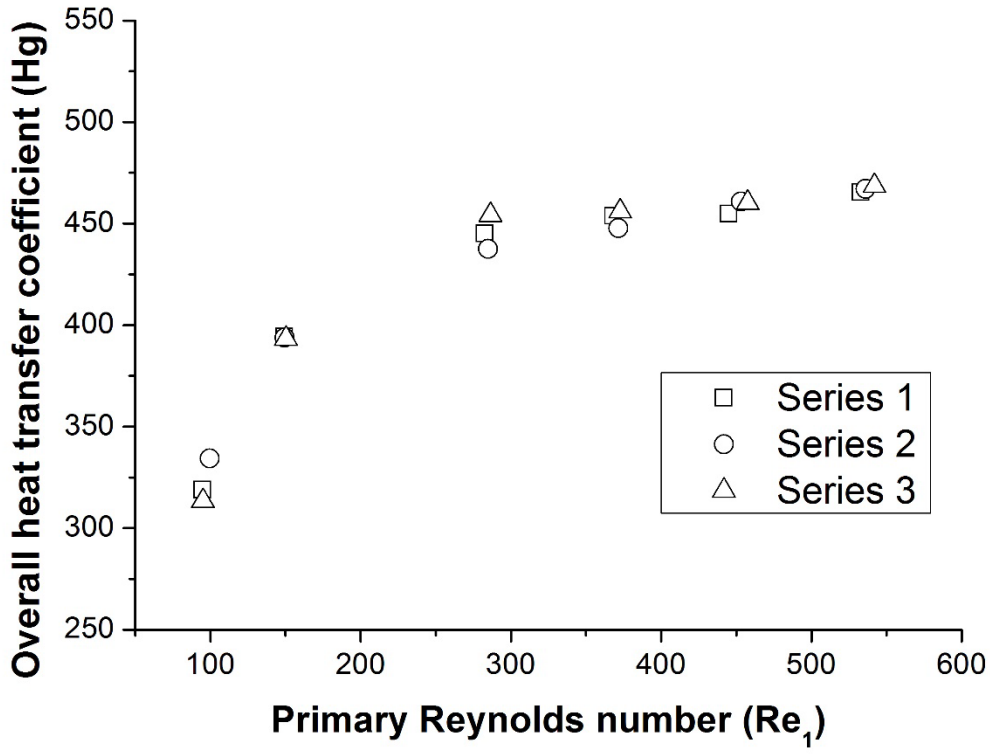

Figure 7: Evolution of the overall heat exchanger coefficient, H_g, versus the primary Reynolds number, Re_1, of the straight tube for three test series

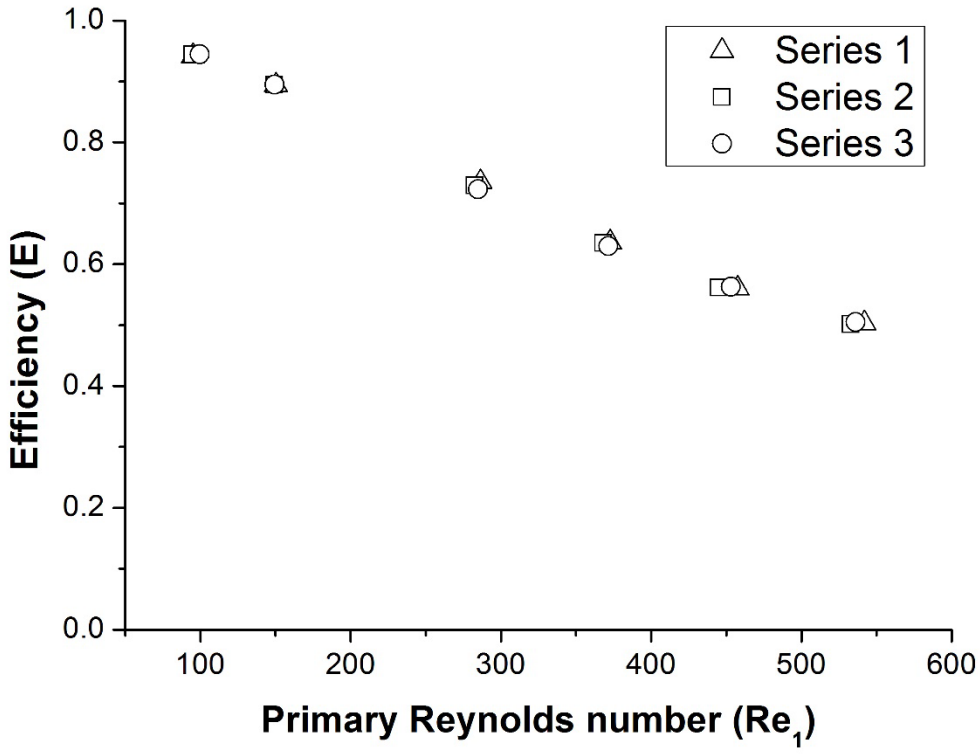

Figure 8: Evolution of the efficiency, E, versus the primary Reynolds number, Re_1, of the straight tube for three test series

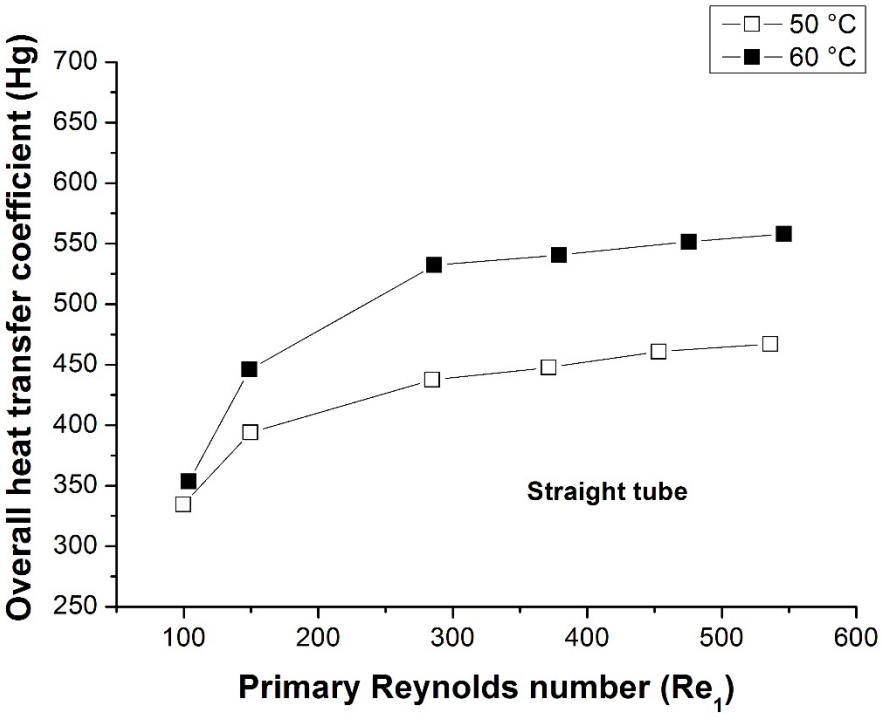

a) straight tube

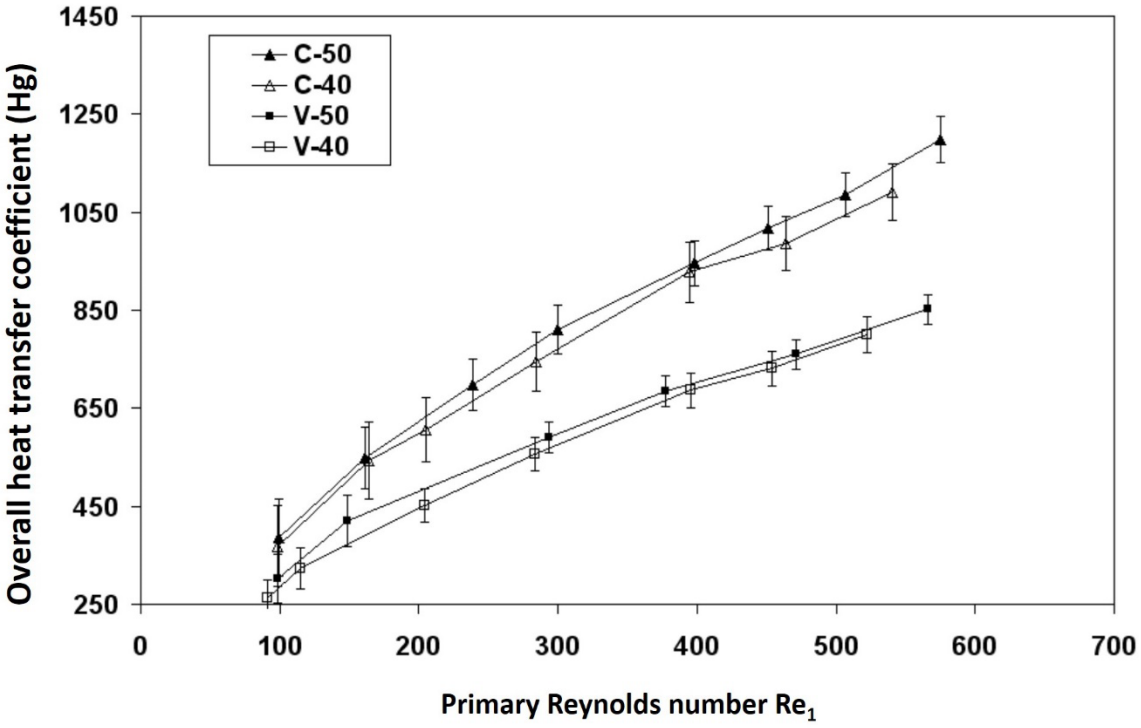

b) chaotic geometries

Figure 9: Evolution of the overall heat exchanger coefficient, H_g, versus the Reynolds number, Re, for two inlet temperatures of the secondary circuit

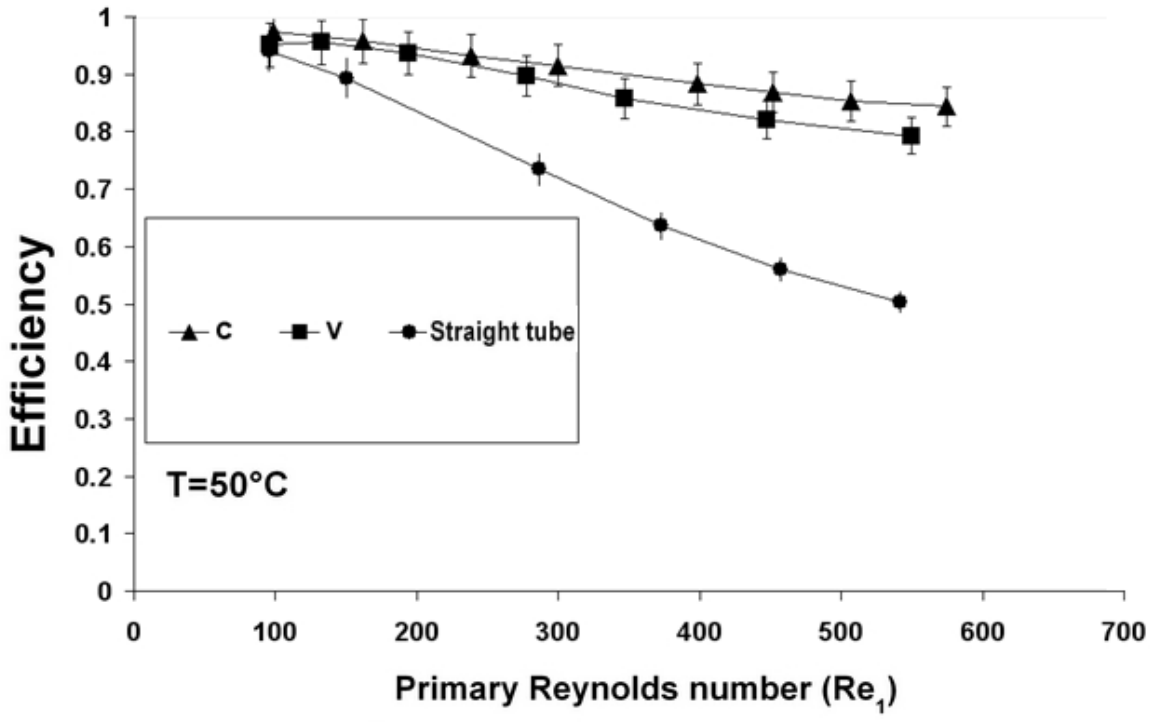

Figure 10: Evolution of the efficiency, E, for the different geometries, straight tube, V and C, versus the primary Reynolds number (Re_1)

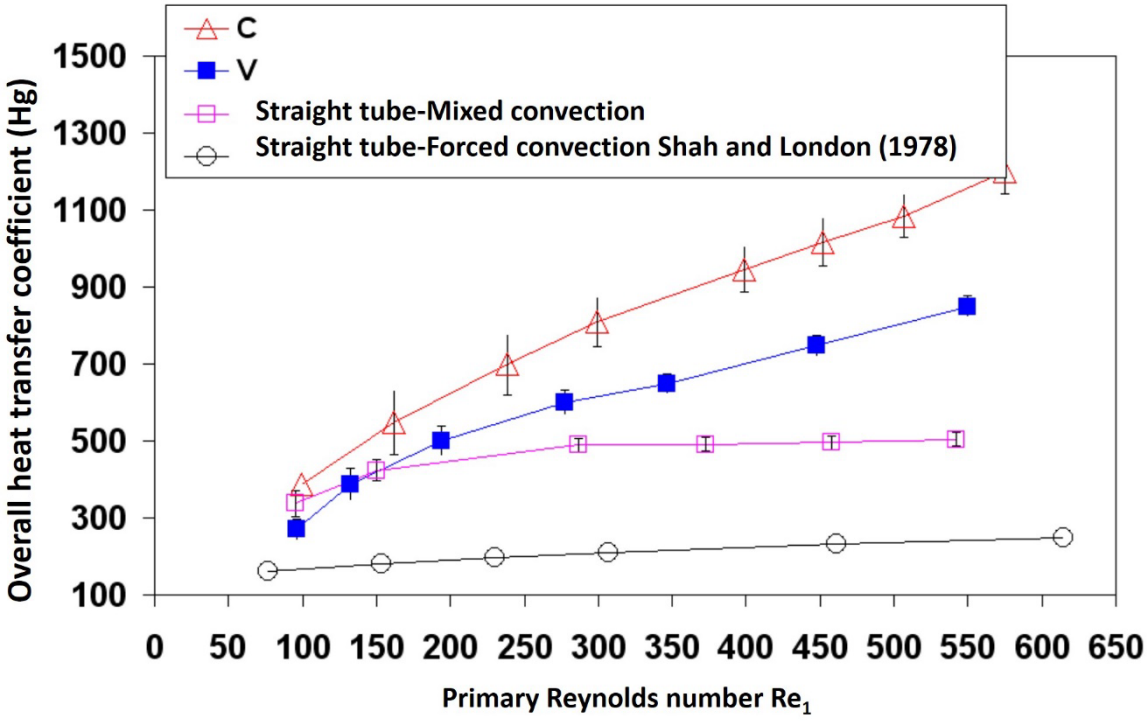

Figure 11: Evolution of the overall heat exchanger coefficient, H_g, versus the primary Reynolds number

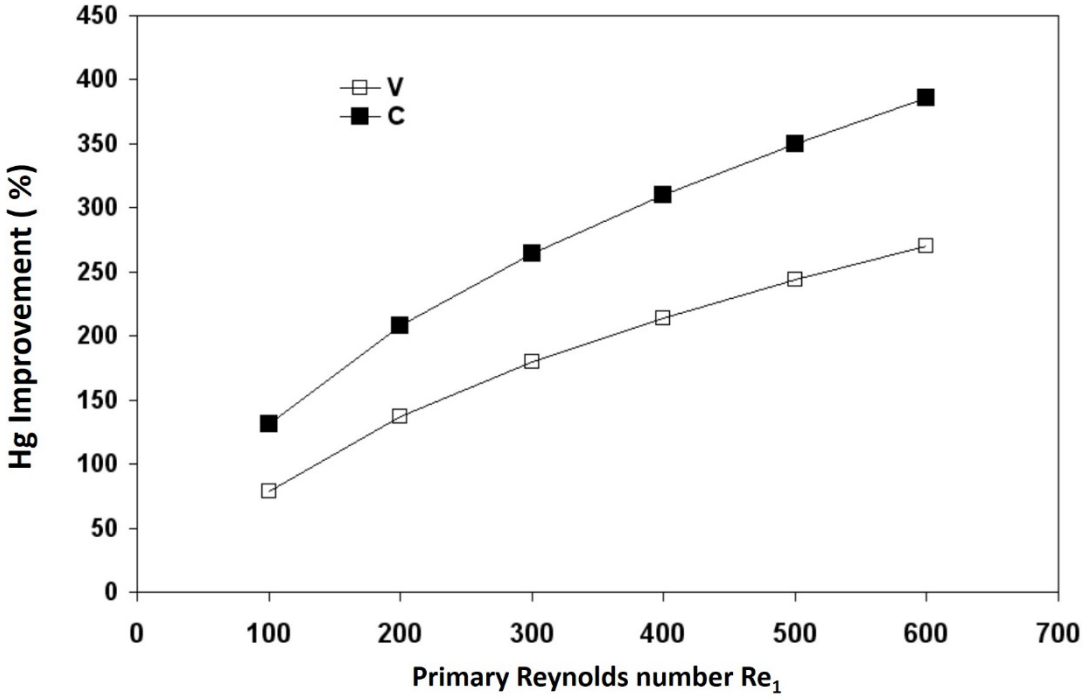

Figure 12: Improvement in the overall heat exchanger coefficient in a chaotic advection regime compared to the regular regime in forced convection (straight tube) versus the primary Reynolds number

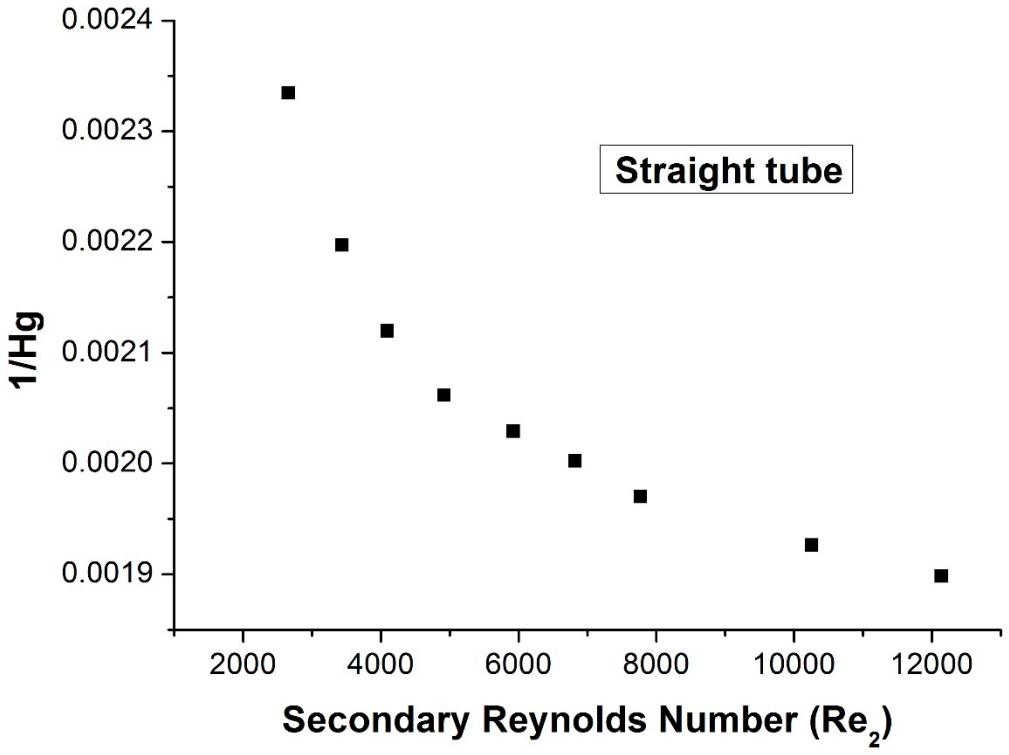

Figure 13: Evolution of the total resistance of the straight duct heat exchanger versus Re_2 (Re_1= 450)

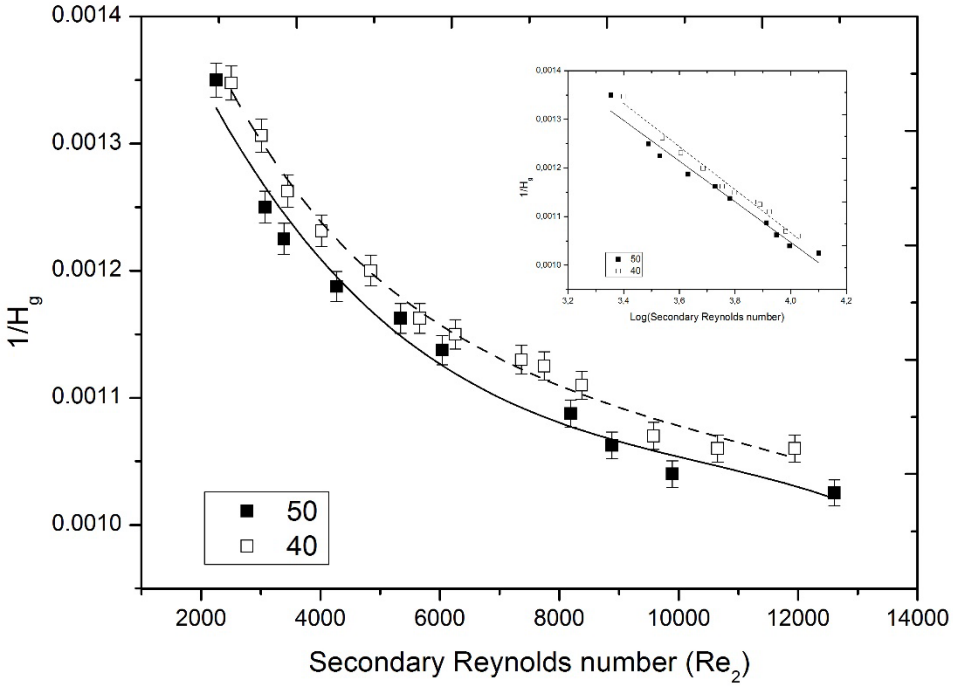

a) Geometry V

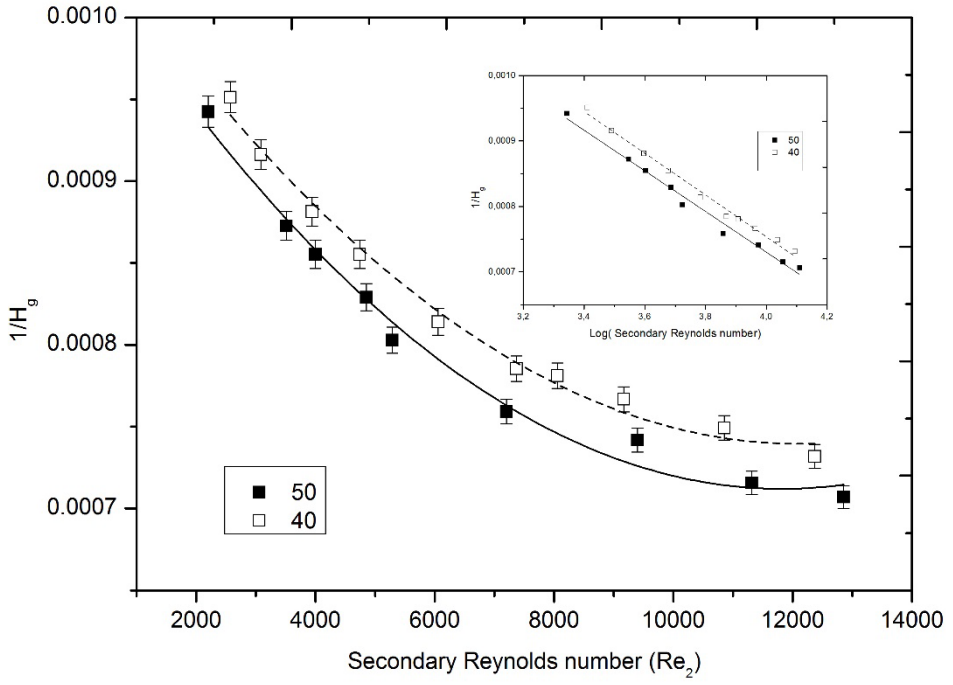

b) Geometry C

Figure 14: Evolution of the heat exchanger total resistance versus Re_s for two inlet temperatures of the secondary fluid (Re_1= 540)